communications chemistry

A Nature Portfolio journal

Article

https://doi.org/10.1038/s42004-026-02121-4

Soluble zinc-induced amyloid β oligomers probed through fluorine NMR spectroscopy

Check for updates

Luigi Russo[1,9], Kalyan S. Chakrabarti[2,9], Robin Backer[3,9], Kerstin Overkamp[4,9], Serge Gambarelli[5], Dieter Willbold[3,6], Giuseppe Sicoli[7] & Nasrollah Rezaei-Ghaleh[8]

Divalent zinc ions (Zn) interact with amyloid β (Aβ) peptides and influence its Alzheimer disease (AD)-related aggregation. Little is known about the structural properties of Zn-induced Aβ oligomers. Here, we report recombinant production of fluorinated Aβ40 at Phe4, Tyr10, Phe19 and Phe20 residues and utilize these fluorinated residues as proxies to interrogate Zn-induced Aβ40 oligomers. Our NMR and CW EPR results confirm Zn binding to the N-terminal region of Aβ40 and demonstrate the reversible oligomerization and irreversible aggregation of Aβ40 upon Zn addition. The ^{19}F NMR relaxation and dark-state exchange saturation transfer (DEST) data provide dynamical information on free Aβ40 and demonstrate that monomeric Aβ40 is in exchange with small Zn-induced Aβ40 oligomers with less than about 60 kDa molecular weight on a millisecond timescale. The ^{19}F ENDOR data suggest that the distance between the N-terminally attached nitroxide spin and fluorinated residues within the Zn-Aβ40 aggregates is larger than about 1.5 nm. Our results shed light on the properties of soluble Zn-induced Aβ oligomers and pave the way for further structural characterization of these Aβ aggregates.

Divalent zinc ions (Zn^{2+}, henceforth Zn) are found in a free or loosely bound form in certain types of synaptic vesicles in the human brain and released into the synaptic cleft of glutamatergic neurons[1], where their concentration can reach ~60 μM[2]. Zinc ions have a propensity to bind the Alzheimer's disease (AD)-related beta-amyloid peptide (Aβ) in the extracellular space and can promote its aggregation[3–5]. These ions are enriched in the AD-related senile plaques and demonstrated in animal AD models to play a role in plaque formation[6–9]. Besides, zinc ion chelation causes dissolution of aggregated Aβ in human brain extracts[10]. Several other aspects of AD and other neurodegenerative diseases can be influenced by Zn, e.g., Aβ cleavage by zinc metalloproteases, tau protein hyperphosphorylation, phase separation and aggregation, neuroinflammation, and synaptic plasticity[11,12]. Moreover, the mutual interference between the redox-silent Zn and redox-active copper (and iron) ions could contribute to their AD-related effects[13].

Due to the potential role of Zn–Aβ complexes in AD pathogenesis, Zn binding and coordination with Aβ have been extensively studied during the past decades using NMR, EPR, X-ray absorption, and other spectroscopic techniques[3,5,14–16]. It is generally accepted that Zn ions primarily bind to the N-terminal 1–16 residues of Aβ with a dissociation constant of ~10 μM and form 1:1 Zn:Aβ complexes[5]. Zn ions are borderline-to-hard Lewis acids and, according to the hard–soft acid–base (HSAB) theory, can easily coordinate in proteins with 4–6 hard (like O), borderline (like N), and sometimes even soft (like S) base ligands provided by one or more protein molecules, in tetrahedral, octahedral, trigonal bipyramidal, and other geometries[17–19]. Considering the intrinsically disordered nature of Aβ and the versatility of Zn coordination in terms of ligand type, number, and geometry, it is not surprising that different coordination models have been suggested for the Zn–Aβ complex depending on Aβ peptide length, sequence mutations and modifications, and Aβ assembly state, as well as experimental conditions such as pH and buffer type and concentration[5]. It is also possible that more than one mode of Zn–Aβ coordination occurs in the same sample. At physiological pH, the side-chain imidazole of the three histidine residues His6, His13, His14, and the N-terminal amine can provide the N ligands, whereas the side-chain carboxylate of Asp1, Glu3, Asp7, and Glu11 can provide the O ligands[3,5,20]. For example, more recent studies have suggested a 2N2O tetrahedral coordination of Zn ions with two histidine residues (His6

[1]Department of Environmental, Biological and Pharmaceutical Science and Technology, University of Campania Luigi Vanvitelli, Caserta, Italy. [2]Department of Biological Science and Chemistry, Krea University, Sri city, Andhra Pradesh, India. [3]Institute of Physical Biology, Heinrich Heine University Düsseldorf, Universitätsstraße 1, Düsseldorf, Germany. [4]Department of NMR-based Structural Biology, Max Planck Institute for Multidisciplinary Sciences, Göttingen, Germany. [5]Univ. Grenoble Alpes, CEA, CNRS, IRIG, SyMMES, Grenoble, France. [6]Institute of Biological Information Processing, IBI-7: Structural Biochemistry, Forschungszentrum Jülich, Jülich, Germany. [7]CNRS UMR 8516, University of Lille, Villeneuve d'Ascq, France. [8]Department of Molecular Medicine, University of Pavia, Pavia, Italy. [9]These authors contributed equally: Luigi Russo, Kalyan S. Chakrabarti, Robin Backer, Kerstin Overkamp e-mail: Nasrollah.RezaieGhaleh@unipv.it

and either His13 or His14) and two carboxylate residues (Glu11 and either Asp1, Glu3, or Asp7) of human Aβ and a 3N1O coordination with murine Aβ[14,15].

Zinc ion binding to Aβ promotes Aβ oligomerization and amorphous aggregation[4,9,21]. In some Aβ mutants, like the H6R mutant in which one of the zinc coordination sites (His6) is substituted, Zn ions induce peptide dimerization in a 1:2 Zn:Aβ complex[22]. Clearly, Zn binding to the N-terminal region of wild-type Aβ induces a rigid structure in this region[20,21], and as suggested before[21], can interfere with the long-range intramolecular interactions between this and distal regions of Aβ crucial for the early kinetics of Aβ fibrillar aggregation[23]. The effect of Zn ions on Aβ aggregation could also occur at sub-stoichiometric ion concentrations, where the lowly-populated Zn-Aβ complex in the monomeric or oligomeric state could potentially act as a template and trigger a template-based Aβ aggregation. Despite their potential importance in relation to AD-related aggregation and toxicity, little is known about the structural properties of Zn-induced Aβ oligomers. This is partly because of the low population of these Aβ oligomers and partly due to their size inaccessibility to standard NMR methods.

Here, we exploit the advantageous properties of spin-half fluorine (^{19}F) nuclei and attempt to overcome these challenges through combining ^{19}F NMR and EPR. To this end, we produce recombinant Aβ40 fluorinated at Phe and Tyr residues or paramagnetic nitroxide spin (MTSSL)-labeled synthetic Cys-Aβ40. The large gyromagnetic ratio (~0.94 of ^{1}H nuclei) and natural abundance (100%) of the introduced ^{19}F nuclei lead to a high sensitivity of ^{19}F NMR experiments and improve their detection limit for the lowly populated soluble Zn-induced Aβ species[24,25]. On the other hand, the use of nitroxide spin label extends the range of accessible length scales within the context of Zn-induced Aβ oligomers and allows monitoring inter-spin distances, whether in the context of small Aβ oligomers or in larger NMR-invisible (but EPR visible) Aβ aggregates. In the presence of equimolar Zn, our ^{19}F NMR relaxation data demonstrate a major monomeric Aβ40 population undergoing exchange with a minor population of Aβ40 oligomers with less than about 60 kDa molecular mass. The ^{19}F ENDOR data suggest that the intermolecular distance between the N-terminal nitroxide spin label and the fluorine-labeled residues (Phe4, Tyr10, Phe19, Phe20) is above ~1.5 nm in the Zn-induced Aβ40 aggregates.

Results

Recombinant production of fluorinated Aβ and assignment of ^{19}F NMR resonances

Previous NMR studies have demonstrated the role of the N-terminal region of Aβ extending up to residue Q15 in interaction with Zn ions, using mainly the NMR probes of Aβ backbone conformation and dynamics such as secondary backbone chemical shifts and ^{15}N relaxation rates[14,20,21]. To further investigate the Zn–Aβ interaction, we decided to incorporate fluorine labels at aromatic residues Phe4 and Tyr10 in the N-terminus, as well as residues Phe19 and Phe20 in the middle of Aβ, and exploit the advantages of ^{19}F NMR. To this end, the fluorinated Aβ40 was prepared recombinantly using *E. coli* DL39(DE3) cells auxotrophic for Phe and Tyr in a defined medium supplemented with 4-fluoro-Phe and 3-fluoro-Tyr (Fig. S1)[26,27]. The recombinantly-produced fluorinated Aβ40 showed the four expected signals in the 1D ^{19}F NMR spectrum, three in the region around −117 ppm typical for 4-fluoro-Phe and one at −138 ppm typical of 3-fluoro-Tyr (Fig. 1B, C). In addition, the NOE-based ^{1}H,^{19}F correlation spectrum (HOESY) showed the expected correlation peaks between ^{19}F and nearby aromatic protons of 4-fluoro-Phe (Hε) and 3-fluoro-Tyr (Hδ) residues (Fig. 1D, E). Subsequently, we chemically synthesized fluorinated Aβ40 at these four residues or site-specifically at positions Phe4, Phe19, or Phe20 (Figs. S2–S5). The 1D ^{19}F NMR spectra of these peptides allowed unequivocal assignment of the three observed ^{19}F NMR signals around −117 ppm (Fig. 1F). The secondary Hα chemical shift analysis of non-fluorinated and fluorinated Aβ40 confirmed that the backbone conformation of Aβ40 was not perturbed by its fluorination (Fig. S6). Furthermore, the ^{1}H-based pulse-field-gradient (PFG) NMR diffusion experiment yielded a diffusion coefficient of $9.18 \pm 0.10 \times 10^{-11}$ m^2 s^{-1} for fluorinated Aβ40 and $4.34 \pm 0.03 \times 10^{-10}$ m^2 s^{-1} for DSS as an internal reference (Fig. 1G). Considering a hydrodynamic radius (R_h) of 0.41 ± 0.01 nm for DSS, the R_h of fluorinated Aβ40 is 1.94 ± 0.05 nm, which closely matches the R_h value measured for non-fluorinated Aβ40 (1.87 ± 0.02 nm, Fig. S7A) and previous reports consistent with a monomeric Aβ state[28]. This suggests that fluorination has not altered the overall size and shape of Aβ40. Besides, it does not impair its capability to form Thioflavin T (ThT)-reactive amyloid fibrils (Fig. S8).

^{19}F relaxation-based dynamics of aromatic rings

Subsequently, we studied the fast dynamics of fluorine-labeled aromatic rings of Aβ40 through ^{19}F NMR longitudinal (R_1) and transverse (R_2) relaxation rates. The R_1 rates were measured through standard inversion-recovery experiments (Fig. 2), whereas the R_2 rates were determined through "dark-state" exchange saturation transfer (DEST) NMR measurements at four ^{19}F B_1 fields of 500, 250, 125, and 62.5 Hz (Fig. 3A)[29]. The DEST data were analyzed assuming a "no exchange" model, yielding R_2 rates. The ^{19}F R_1 and R_2 rates are mainly determined by the ^{19}F chemical shift anisotropy (CSA) and ^{1}H,^{19}F dipole-dipole coupling (DD) relaxation mechanisms, hence their alterations report changes in the electronic environment of aromatic ring-attached fluorine atoms and their rotational correlation times (τ_c) (Fig. S9)[25]. The ^{19}F R_1 rates of Phe4, Phe19, and Phe20 of free Aβ40 were 1.50 ± 0.03, 1.46 ± 0.04 and 1.45 ± 0.04 s^{-1}, respectively, and that of Tyr10 was 1.75 ± 0.03 s^{-1} (Fig. 2A–D). The corresponding ^{19}F R_2 rates derived from the DEST data of free Aβ40 were 8.9 ± 0.1, 10.5 ± 0.2, and 11.6 ± 0.2 s^{-1}, respectively for Phe4, Phe19, and Phe20, and 18.8 ± 0.3 s^{-1} for Tyr10 (Fig. 3A–D). The obtained ^{19}F R_1 and R_2 relaxation rates could be reproduced with a τ_c of 0.90–1.14 ns for Phe and ~1.17 ns for Tyr, combined with a (reduced) ^{19}F CSA of ~56–59 ppm for Phe and 76–77 ppm for Tyr residues (Table 1). The obtained τ_c values are consistent with the sign of NOE cross-peaks between the aromatic side chains (Fig. S10), putting a lower limit of ~0.3 ns for τ_c (at proton Larmor frequency of 600 MHz), and combined with the diffusion data (see above), are compatible with a monomeric Aβ state[28,30]. Also, the estimated ^{19}F CSA values are in reasonable agreement with previous reports for these fluorinated amino acids[31,32].

^{19}F NMR spectra confirm binding of Zn ions to the N-terminal region of Aβ

Next, we studied Zn binding to recombinantly-produced fluorinated Aβ40. First, the use of HEPES as buffer was shown to cause a near-complete loss of the NMR signals of Aβ40 at Zn:Aβ40 ratio of 1:1 (Fig. S11). Therefore, we shifted to phosphate (10 mM), where a significant fraction of Zn is expected to be bound to phosphate, and therefore, the effective Zn concentration would be smaller than its nominal concentration. Notably, at pH 7.4 and 278 K, the predominant phosphate species are expected to be HPO_4^{2-} and $H_2PO_4^{-}$, with PO_4^{3-} concentration being much smaller within the nM range. Upon addition of 100 μM $ZnCl_2$, the complexation of Zn^{2+} ions with these species (predominantly with HPO_4^{2-}, as $ZnHPO_4$ and $Zn(HPO_4)_2^{2-}$) brings down the free Zn^{2+} ion concentration to ~7.5 μM, lower than the estimated limit for amorphous precipitation of $Zn_3(PO_4)_2$ under this condition (after taking activity corrections into account). Accordingly, no evidence of zinc phosphate particle formation larger than 1 nm was observed in dynamic light scattering (DLS) measurements at this temperature (Fig. S12). At nominal 1:1 and especially 2:1 Zn:Aβ40 ratios in 10 mM phosphate (henceforth only nominal Zn concentrations and ratios are reported), a general intensity reduction was observed in 1D ^{1}H NMR spectra, indicating a Zn-induced conversion of Aβ40 to NMR-invisible aggregates (Fig. S13). In 2D ^{1}H,^{1}H TOCSY spectra, the intensity reduction of H_N/Hα cross-peaks was more pronounced in the N-terminal region of Aβ up to residue Lys16, consistent with the primary binding of Zn to this region (Fig. S14). In addition, significant H_N/Hα chemical shift perturbations, larger than the average value plus standard deviation, were observed for Glu3, Arg5, His6, Asp7, and Gly9, indicating that the Zn binding induces local conformational

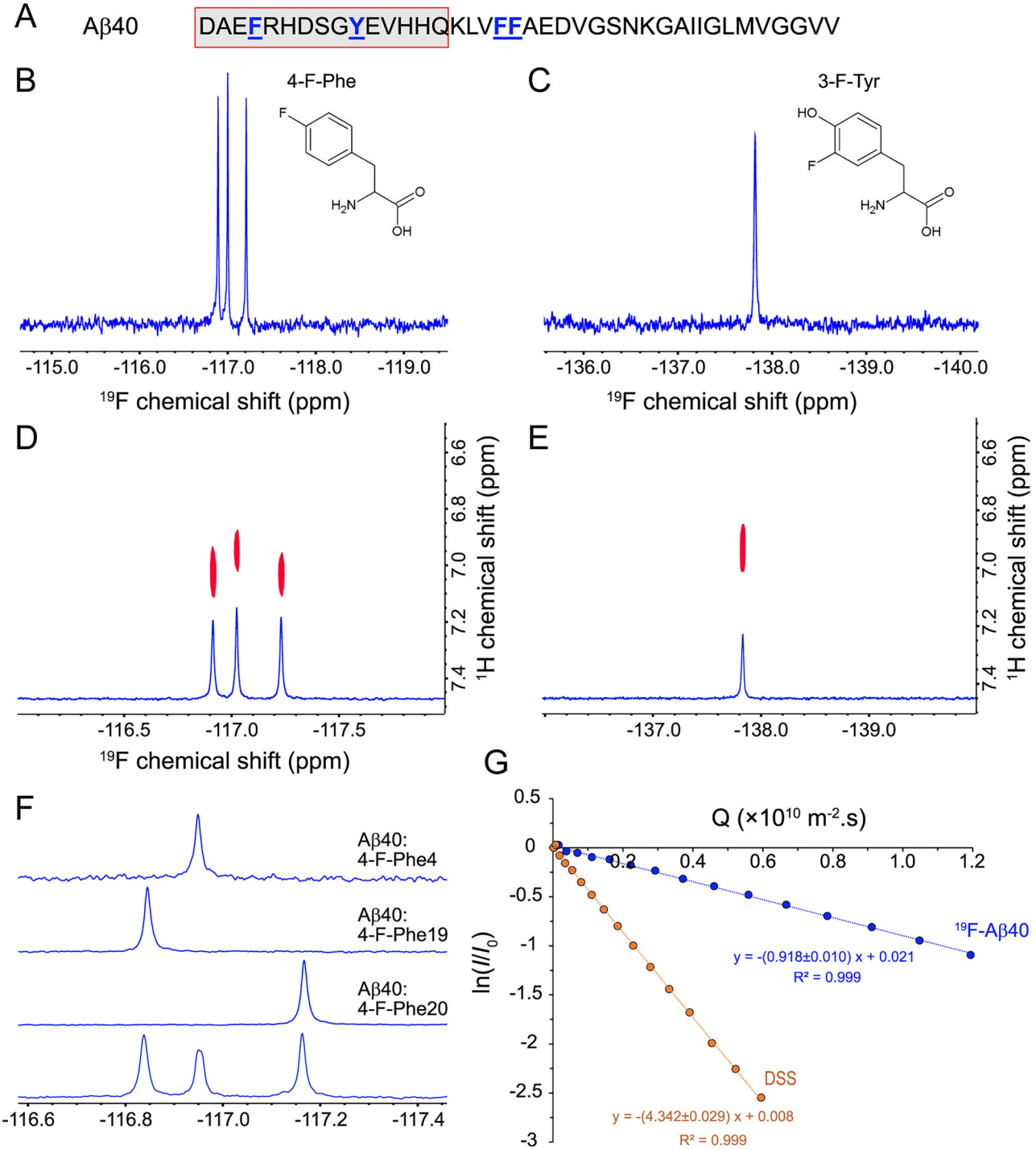

Fig. 1 | NMR-based characterization of fluorinated Aβ40. A Aminoacid sequence of Aβ40. The shaded box highlights the N-terminal region of Aβ40 involved in zinc ion binding. The fluorine-labeled residues F4, Y10, F19, and F20 are underlined. **B**, **C** 1D ^{19}F spectrum of recombinantly produced fluorinated Aβ40, showing the expected three signals around −117 ppm typical of 4-F-Phe and one around −138 ppm typical of 3-F-Tyr. The 2D chemical structures of 4-F-Phe and 3-F-Tyr are shown. **D**, **E** 2D ^{1}H,^{19}F HOESY spectrum of recombinantly produced fluorinated Aβ40, showing correlation between ^{19}F signals and the nearest aromatic proton signals. **F** 1D ^{19}F spectrum of chemically synthesized fluorinated Aβ40, with fluorine labels incorporated at three Phe (and Tyr) residues (bottom) or with site-specific ^{19}F labeling exclusively at Phe4, Phe19, or Phe20. **G** Pulse-Field-Gradient (PFG) NMR diffusion data of recombinantly produced fluorinated Aβ40, along with an internal reference, DSS. The comparison between apparent diffusion coefficients of fluorinated Aβ40 and DSS allows the determination of the hydrodynamic radius for fluorinated Aβ40 (~1.94 nm), consistent with a monomeric Aβ40 state.

rearrangements of the metal binding region (Fig. S14). Besides, residues Arg5, His6, Asp7, Glu11, His13, and His14 showed a strong intensity reduction of side-chain and aromatic proton signals upon addition of Zn (Fig. S15). Interestingly, the intensity reduction observed for the HN/Hγ cross-peak of Glu11 was more pronounced than its HN/Hβ cross-peak (Fig. S15), in line with a recent 2N2O coordination model in which the carboxylate group of Glu11 is involved in Zn coordination in addition to the carboxylate group of Asp1 and imidazole rings of two Histidines[14]. Notably, the sequence profile of backbone intensity perturbations was highly similar and the level of Zn-induced Aβ aggregation was comparable in 10 mM Tris-

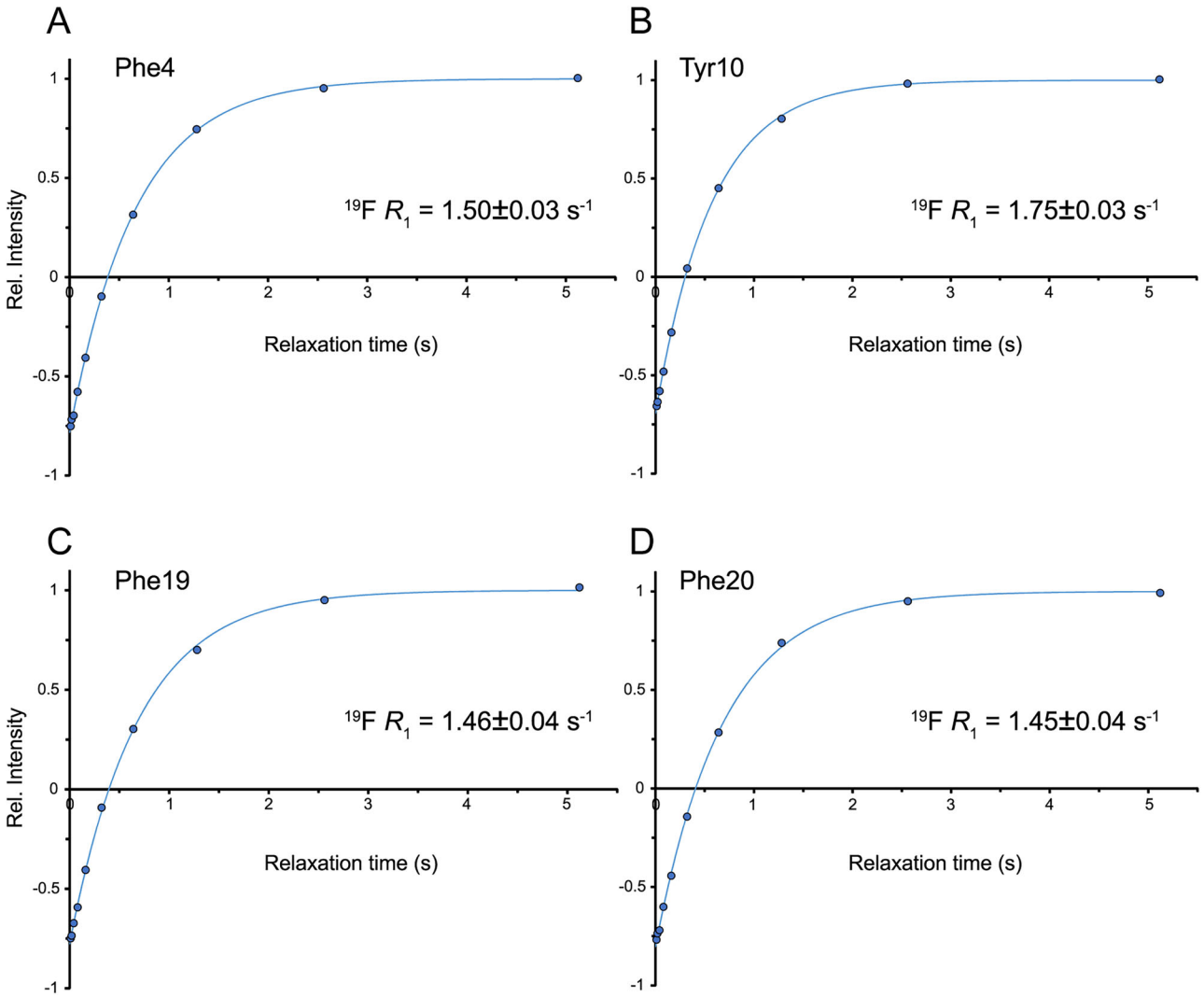

Fig. 2 | ^{19}F longitudinal spin–lattice (R_1) relaxation rates of fluorinated Aβ40. The R_1 rates were measured through inversion–recovery experiments, for residues Phe4 (**A**), Tyr10 (**B**), Phe19 (**C**), and Phe20 (**D**). The fluorine atoms are substituted at position 4 (*para*) of Phe and 3 (*meta*) of Tyr aromatic rings.

HCl buffer at pH 7.4, indicating that the observed effects are induced by Zn^{2+} ion binding independent of buffer type (Fig. S16).

In 1D ^{19}F NMR spectra, after addition of Zn to Aβ40 at 1:1 and 2:1 ratios, a clear decrease in ^{19}F signal intensities was observed for all four signals (Fig. S17). The relative intensity reduction was, however, more pronounced for Phe4 and to a lower extent Tyr10, compared with Phe19 and Phe20 (Fig. 4). Similarly, a differential intensity reduction effect was observed after addition of Zn to synthetic fluorinated Aβ40, with Phe4 and Tyr10 exhibiting more significant intensity loss (Fig. S18). The ^{19}F chemical shifts did not show a significant perturbation after addition of Zn ions, in line with a slow-exchange regime of binding with respect to NMR chemical shift timescale. Interestingly, after the addition of an excess amount of EDTA (5 mM, incubation time 2–3 h), a Zn chelator, the ^{19}F signal intensities were partially recovered (Fig. S17) and the relative ^{19}F signal intensity profile was resumed (Fig. 4). These results indicate that the Zn-induced Aβ aggregates are composed of two sub-populations, only one of them is reversible upon Zn chelation. Overall, these data provide further support for the binding of Zn to the N-terminal region of Aβ40, affecting, e.g., residues Phe4 and Tyr10, whereas distal residues Phe19 and Phe20 remain largely unaffected. The Zn binding to Aβ40 induces Aβ oligomerization/aggregation, which is partially reversible. Notably, the size-exclusion chromatography (SEC)-based data showed a similar level of Zn-induced aggregation for non-fluorinated and fluorinated Aβ40 (see Supplementary Methods and Results and Fig. S19).

Next, we investigated the effect of Zn addition on Aβ40 diffusion through PFG-NMR measurements before and after addition of Zn (Zn:Aβ40 ratio of 2:1). The obtained diffusion coefficient of non-fluorinated Aβ40 in the absence of Zn ($9.06 \pm 0.10 \times 10^{-11}$ m^2 s^{-1}, Fig. S7A) and its calculated R_h (1.87 ± 0.02 nm) closely matched those of fluorinated Aβ40 (see above, Fig. 1G). Upon addition of Zn, the diffusion coefficient of the internal reference DSS showed ~10% reduction (Fig. S7B), potentially reflecting an increase in sample viscosity due to Zn-induced Aβ aggregation. Interestingly, the apparent R_h of Aβ40 increased to 2.06 ± 0.04 nm, showing an increase of 10 ± 2% with respect to free monomeric Aβ40. This increase in R_h cannot be explained by the formation of monomeric Zn–Aβ complex, because mere binding of Zn to the N-terminal region of Aβ40 without further aggregation is expected to induce a less extended structure in Aβ40 and reduce its R_h. Instead, the increase in R_h suggests Zn-induced formation of Aβ40 oligomers in fast exchange with NMR-visible Aβ40 monomers at NMR diffusion timescale (see below for further information).

CW EPR-based evidence of Zn binding to Aβ

Large Aβ40 aggregates induced by Zn are not accessible to the NMR methods employed above, because of their large size and the consequent broadening of their signals beyond NMR detection. To further monitor the effect of Zn binding on Aβ40, we prepared MTSSL-labeled Cys-Aβ40 for Electron Paramagnetic Resonance (EPR) studies. The inspection of 2D

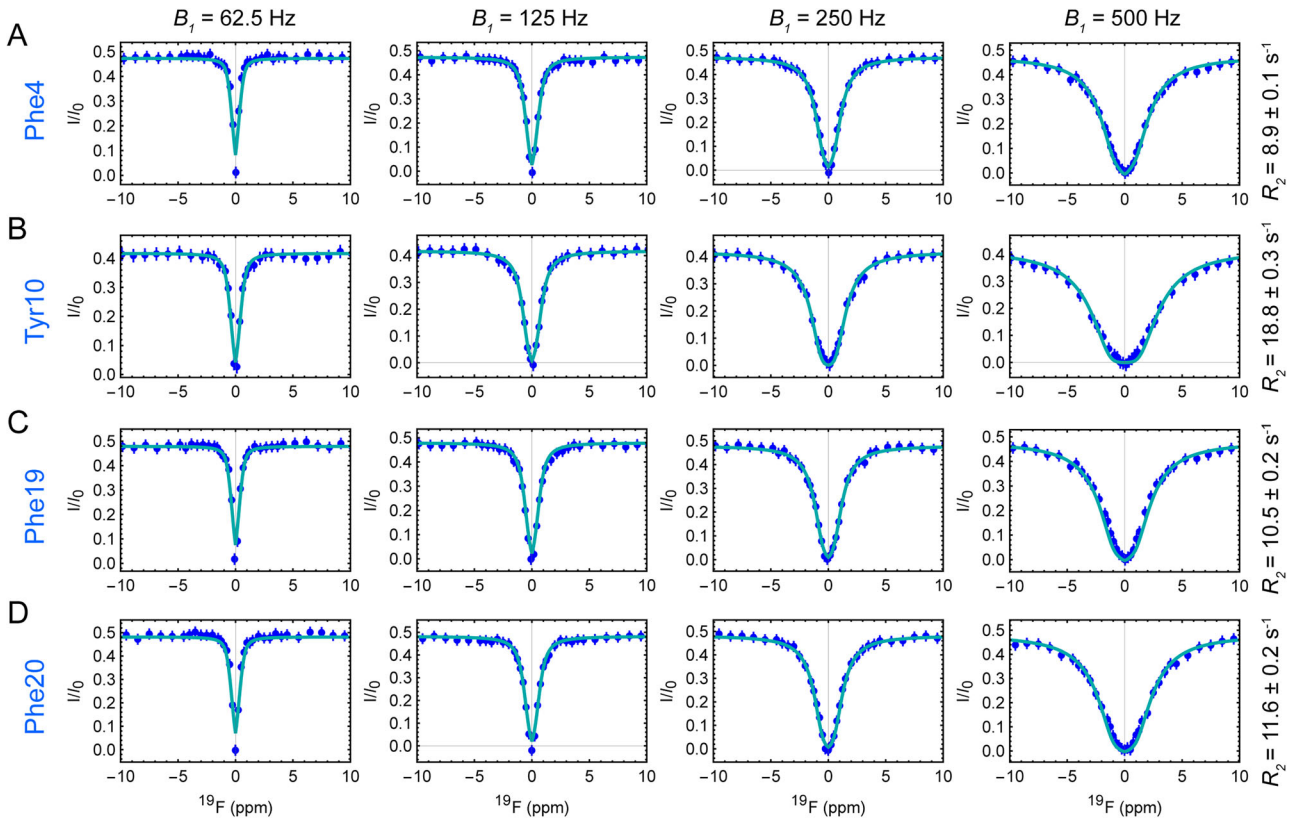

Fig. 3 | ^{19}F transverse spin–spin (R_2) relaxation rates of fluorinated Aβ40. The R_2 rates were measured through ^{19}F DEST experiments at four ^{19}F B_1 fields of 62.5, 125, 250, and 500 Hz, for residues Phe4 (**A**), Tyr10 (**B**), Phe19 (**C**), and Phe20 (**D**). The DEST profiles were acquired for the free Aβ40, i.e., in the absence of zinc ion, and analyzed assuming a "no exchange" model. The fluorine atoms are substituted at position 4 (*para*) of Phe and 3 (*meta*) of Tyr aromatic rings. The fitted R_2 values are shown on the right for each residue, representing the estimated mean values, with standard errors of fits shown as uncertainties. The uncertainties in the data points are the standard deviation of independent experimental measurements ($n = 10$) at different ^{19}F chemical shifts, where the DEST profile is flat. The maximum of the individual values from 62.5 Hz and 125 Hz B_1 fields has been used for all other data (where the flat portion was not evident). The error bars (reflecting the standard deviation of $I/I_0 = 0.02$) are centered around the measured I/I_0 ratio, where I and I_0 are the peak intensities with and without relaxation during the DEST delay, respectively.

Table 1 | The ^{19}F longitudinal (R_1) and transverse (R_2) relaxation rates, rotational correlation time (τ_c), and reduced anisotropy (δ_σ) of Aβ40 peptide in the free and zinc ion (Zn)-bound states, determined from ^{19}F inversion–recovery and DEST measurements

	Free				Zn-bound			
	R_1 (s^{-1})	R_2 (s^{-1})	τ_c (ns)	δ_σ (ppm)	R_1 (s^{-1})	R_2 (s^{-1})	τ_c (ns)	δ_σ (ppm)
Aβ40					$k_{ex} = 1022 \pm 60$ s^{-1}, $P_B = 11.6 \pm 0.1$%			
Phe4	1.50 ± 0.03	8.9 ± 0.1	0.90 ± 0.01	56.0 ± 0.1	0.06 ± 0.02 [a]	152 ± 2	15 ± 2	60 ± 5
Tyr10	1.75 ± 0.03	18.8 ± 0.3	1.17 ± 0.02	76.6 ± 0.7	–[b]	–	–	–
Phe19	1.46 ± 0.04	10.5 ± 0.2	1.04 ± 0.02	58.4 ± 0.5	0.05 ± 0.02 [a]	76 ± 1	7 ± 1	63 ± 6
Phe20	1.45 ± 0.04	11.6 ± 0.2	1.14 ± 0.02	58.2 ± 0.4	1.00 ± 0.07 [a]	59 ± 1	7 ± 1	55 ± 5

[a]Due to the small contribution of the R_1 of the lowly populated Zn-bound Aβ40 to the DEST profiles, these values were not considered as quantitative estimates and excluded from rotational correlation time and (reduced) anisotropy analysis. They are reported here only for the sake of completeness.

[b]Tyr10 was excluded from the DEST analysis of Aβ40 in the presence of zinc ion because of its suboptimal fit (see Fig. S24).

The population of zinc ion-bound Aβ40 (P_B) and the exchange rate between the free and zinc ion-bound states (k_{ex}) derived for the sample containing equimolar zinc ion and Aβ40 are shown.

^{1}H,^{1}H TOCSY NMR spectra confirmed the incorporation of the paramagnetic MTSSL probe at the N-terminus of Aβ40 (Fig. S20). The signal intensity data showed the expected intramolecular paramagnetic relaxation enhancement (PRE)-induced complete loss of intensity for the N-terminal residues up to Asp7 adjacent to the MTSSL nitroxide spin and a significant intensity reduction for residues Ser8–Tyr10. Interestingly, the segment Gln15–Phe19 exhibited a considerable level of intensity reduction, suggesting the spatial proximity between this segment and the N-terminal MTSSL nitroxide spin within the Aβ ensemble (Fig. S20). Furthermore, the 1D ^{1}H NMR spectra showed that MTSSL incorporation at Cys0 did not interfere with the Zn binding to the N-terminus of Aβ40 (Fig. S21).

EPR methods can access the paramagnetic probe, here the nitroxide spin probe of MTSSL, irrespective of the assembly state of the tagged protein. To avoid the nitroxide exchange interactions, the MTSSL-labeled Aβ was diluted with equimolar non-fluorinated Aβ40 (sample I) or fluorinated Aβ40 (sample II). The CW EPR provides information on the reorientational dynamics of the nitroxide moiety of the MTSSL label, which are generally influenced by the local sidechain and backbone dihedral angle fluctuations,

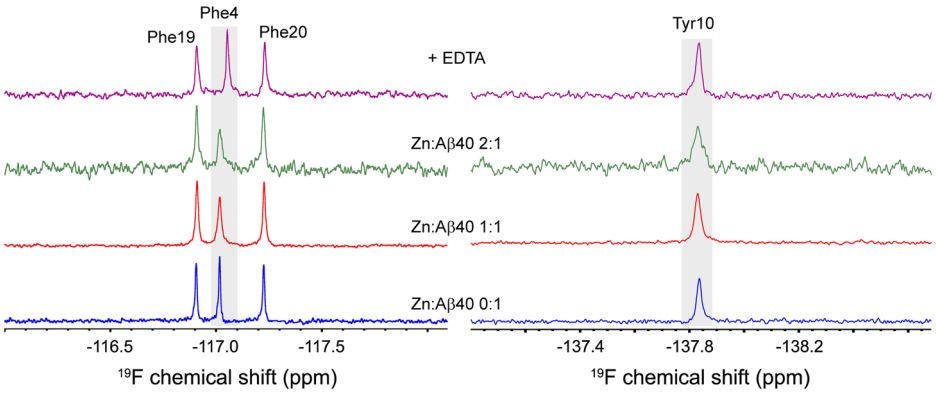

Fig. 4 | Effect of zinc ion on the 1D ^{19}F NMR spectra of fluorinated Aβ40. The spectra are shown in ^{19}F-Phe (left) and ^{19}F-Tyr (right) regions, in the absence or presence of zinc ion at Zn:Aβ40 ratio of 1:1 or 2:1, indicating the relative intensity reduction for residues Phe4 and Tyr10. After the addition of a chelating agent (EDTA), the relative intensities of ^{19}F signals are recovered. The observed change in the chemical shift of Phe4 is probably due to a slight pH change after the addition of 5 mM EDTA and the resultant alteration in the protonation state of the nearby His6's side chain.

as well as the global tumbling of the protein. The CW spectra of samples I and II showed the typical nitroxide-type radical species with two different components, the fast component with three narrow lines (linewidth, 3.0 mT) and the slow component with one broad line (linewidth, 7.0 mT) (Fig. 5A, B). Upon addition of Zn, the broad component exhibited a significant increase in both samples (Fig. 5C, D). The simulation of CW spectra suggested an increase in the slow-motion component from 78% to 94% (Fig. S22). Correlation times for those two components are 4 ns and 10 ns, respectively, associated with spectral widths of 3.2 and 7.0 mT. The CW data provide further support for the Zn binding at the N-terminal region of Aβ40, which leads to relative rigidification of this region, whether they are parts of Aβ40 monomers, dimers, or larger oligomers. However, since no ^{19}F NMR chemical shift perturbation or the emergence of new peaks was observed (see above, Figs. 4, S17, and S18), the significant formation of dimers or other NMR-visible small oligomers could be excluded.

^{19}F ENDOR-based investigation of inter-spin distances

The fluorinated Aβ provides a unique opportunity to measure inter-spin distances upon addition of Zn, if the MTSSL is in close proximity to the ^{19}F-labeled residues (<1.5–2.0 nm)[33,34]. To this end, ^{19}F Mims ENDOR was recorded on the two samples analyzed above (samples I and II, before and after addition of Zn). ^{19}F Mims ENDOR spectra were recorded at Q-band (34 GHz), taking advantage of superior concentration sensitivity. As shown in Fig. 6, at Q-band, only ^{1}H ENDOR signals were detected, with a Larmor frequency centered at 50.95 MHz and two main hyperfine splittings (for two sets of ^{1}H coupled nuclei). The unmodified spectral region centered at the ^{19}F Larmor frequency 47.92 MHz is highlighted by a blue arrow. This supports the lack of ^{19}F signal detection and suggests distances of > 1.5 nm between the MTSSL nitroxide (NO•) and ^{19}F nuclear probes[33]. A similar pattern was observed in HEPES buffer (Fig. S23), supporting that the lack of ^{19}F signal detection was independent of the buffer type used. Thus, while the interaction with Zn ions is validated by NMR and CW EPR data, the undetectable ^{19}F/NO• hyperfine coupling supports long distances between residues containing ^{19}F and the N-terminal paramagnetic species within the Zn-induced Aβ aggregates.

DEST data demonstrate the effect of Zn binding on Aβ dynamics

To investigate the exchange dynamics of Aβ40 between the free and Zn-bound states, we employed the ^{19}F DEST experiments. In ^{19}F DEST experiments, a relatively weak ^{19}F radiofrequency (RF) irradiation (B_1) applied for a relatively long time causes partial signal saturation of a large NMR-invisible ("dark") minor state (here Zn-induced Aβ oligomers), which after exchange with a smaller NMR-visible major state (here Aβ monomers) and the consequent transfer of signal saturation, leads to NMR signal attenuation in dependence of the applied RF frequencies. The DEST experiments are based on a large R_2 difference between the exchanging states, and their parameters, such as RF B_1 field strength and frequencies, are optimized for the determination of the R_2 of the large species, while the chemical shift information for the large species often remains unavailable. In the absence of Zn, the ^{19}F relaxation and DEST experiments analyzed under the no-exchange model yielded the ^{19}F R_1 and R_2 rates for each fluorine-labeled residue consistent with a monomeric Aβ state (see above, Fig. 3). In the presence of Zn, the DEST experiment allowed accessing the otherwise NMR-invisible Zn–Aβ40 complex and provided the ^{19}F relaxation rates in the bound state (Table 1), as well as its population and the exchange rate between the free and Zn-bound states. The ^{19}F DEST profiles obtained for three Phe residues showed a satisfactory fit with the "two-site exchange" model, allowing a semi-quantitative analysis of DEST data (Fig. 7). The quality of fit was less satisfactory for Tyr10 (Fig. S24). This is possibly due to the additional ring flip motion experienced by the fluorine nuclei at the *meta* position of Tyr rings. In contrast, the Phe residues are unaffected by the ring flip motion since the fluorine nuclei are at the *para* position. Therefore, fluoro-Tyr residues are not amenable to a simple two-site exchange model and are excluded from further DEST analysis. In general, the broader ^{19}F DEST profiles of the Zn-containing Aβ sample (Fig. 7) compared to those of the Zn-free sample (Fig. 3) indicate an exchange process occurring between Aβ monomers and larger Zn-induced oligomers. The R_2 of the Zn-induced Aβ oligomers was calculated by fitting the DEST profiles to a two-site (global) exchange model, in which the exchange process was (for the sake of analysis) assumed to occur between the monomeric Aβ and a single oligomeric state. In ~100 μM Aβ40 sample containing equimolar Zn ion, the global fit of DEST data for three Phe residues yielded a population (P_B) of the exchanging Zn–Aβ40 state as 11.6 ± 0.1% and the exchange rate (k_{ex}) between the free and Zn–Aβ40 states as 1022 ± 60 s^{-1}. Considering that the 1D ^{1}H NMR-based population of free Aβ40 was ~74% at 1:1 Zn:Aβ40 ratio (estimated through NMR signal intensities in the methyl region over 0.8-1 ppm, see Fig. S13), the concentrations of free Aβ40 and the exchanging Zn–Aβ40 complex were estimated at ~74 and 9 μM, respectively. That leaves ~18 μM for irreversible Zn-induced Aβ40 aggregates, which do not exchange with the NMR visible Aβ40 monomers. It should be remembered that the effective Zn:Aβ40 ratio in phosphate buffer is smaller than the nominal 1:1 ratio, which is in line with the sub-stoichiometric concentration of Zn-induced Aβ40 aggregates. Furthermore, it is possible that Zn:Aβ stoichiometry within Zn–Aβ40 aggregates is smaller than 1, which would fit an even smaller effective Zn concentration in phosphate buffer. Assuming the above concentrations for the two exchanging states, the obtained k_{ex} indicates a dissociation rate (k_{off}) of 916 ± 54 s^{-1}, indicating a millisecond timescale lifetime for the Zn–Aβ40 complex. In addition, the forward rate is estimated at 106 ± 81 s^{-1}, in reasonable agreement with previous fluorescence-based stopped flow measurements[35]. Regarding ^{19}F relaxation rates in the exchanging Zn–Aβ40 complex (Table 1), the largest R_2 was obtained for Phe4 (152 ± 2 s^{-1}), in line with the direct binding of Zn to the N-terminal region of Aβ40 and the consequent rigidification of these residues. Lower R_2 rates of 76 ± 1 and 59 ± 1 s^{-1} were obtained for Phe19 and Phe20. Interestingly, the R_2 of Phe4 could be reproduced with a combined τ_c of 15 ± 2 ns and (reduced) ^{19}F CSA of 60 ± 5 ppm. At 278 K, and assuming

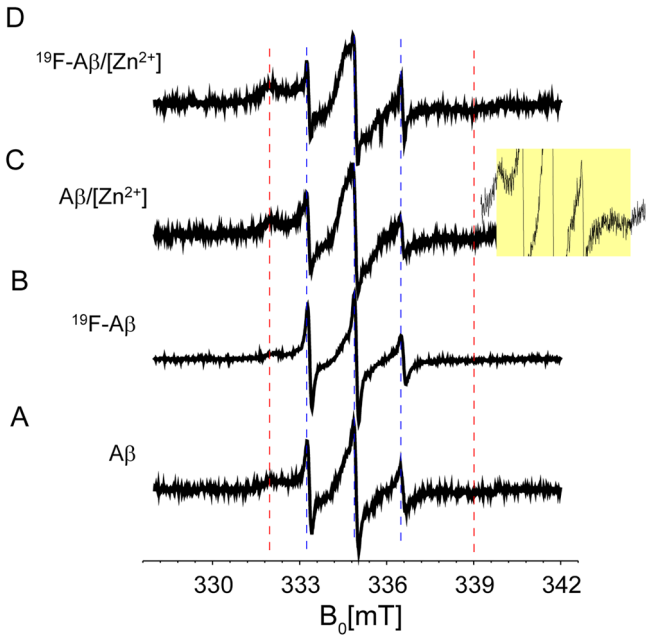

Fig. 5 | Effect of zinc ion on the continuous-wave (CW) EPR spectra of Aβ40. The CW spectra were recorded at room temperature (295 K) for **A** Aβ40, **B** ^{19}F-Aβ40, **C** Aβ40/[Zn] (1:1), and **D** ^{19}F-Aβ40/[Zn] (1:1). Each Aβ sample contains a 1:1 mixture of MTSSL-labeled Cys-Aβ40 and non-fluorinated (**A**, **C**) or fluorinated (**B**, **D**) Aβ40. The addition of Zn leads to an increase in the broad component of the MTSSL nitroxide signal. The zoom in panel **C** highlights the broad (and slow) component (7.0 mT) of the CW spectrum.

that the exchanging Zn–Aβ40 complex behaves as a rigidly rotating molecule, this value of τ_c imposes a lower limit of 25 ± 4 kDa for its molecular mass, corresponding to oligomers composed of 5–7 Aβ40 molecules. Since residues outside the N-terminal zinc ion-binding site of Aβ40 are unlikely to get completely rigidified (residues 1–16 with the MW of ~1955 kDa, compared with the MW of 4330 kDa for the whole Aβ40 molecule), the actual size of the exchanging Zn–Aβ40 complex is larger than this value and probably lies below 60 kDa. Notably, the exchange between these Aβ oligomers and monomeric Aβ is fast with respect to diffusion timescale; therefore, the apparent diffusion coefficient (or R_h) measured through NMR diffusion experiments should be a population-weighted average of the diffusion coefficients of these exchanging species (or in the case of R_h, their corresponding harmonic average). Accordingly, the observed ~10% increase of R_h after Zn addition (see above) will be consistent with the formation of 10–25% Aβ oligomers with sizes ranging from 5 to 14 Aβ40 molecules, which is in qualitative agreement with the other NMR and SEC data reported above.

Discussion

In line with previous studies, our ^{19}F NMR data indicate that Zn ions primarily bind to the N-terminal region of Aβ40 upstream to Phe19[3,5,20,21]. This is shown by the more pronounced ^{19}F NMR signal intensity reduction observed for Tyr10 and particularly Phe4, compared with those of Phe19 and Phe20 (Fig. 4), and supported by the CW EPR data indicating the relative rigidification of the N-terminally attached MTSSL tag (Fig. 5 and Fig. S22). The binding of Zn to the N-terminal region of Aβ leads to rapid conversion of Aβ monomers to NMR-invisible aggregates and leads to intensity reduction for all four ^{19}F signals and an almost uniform intensity reduction for ^{1}H signals of residues downstream to Val18 (Fig. S14). The additional ^{1}H intensity reduction observed for the N-terminal residues is due to chemical/conformational exchange processes caused by Zn binding. These data, combined with differential ^{1}H intensity reduction observed for several side-chain resonances (Fig. S15), are consistent with a 2N2O coordination model proposed previously[14].

Soluble amyloid oligomers are widely considered as the primary toxic species of amyloidogenic proteins, including Aβ[36], and may play a key role in prion-like spreading of amyloid pathology in human brains[37,38]. It has been previously demonstrated that Zn ions induce off-pathway soluble Aβ oligomers, which exhibit distinct properties from the Aβ-derived diffusible ligands (ADDLs)[39], the on-pathway oligomeric species commonly used in Aβ toxicity studies[40]. Compared to the ADDLs, a previous study has shown that the Zn-induced Aβ oligomers are less heterogeneous in size, expose more hydrophobic surface patches, exhibit less immunoreactivity with anti-Aβ antibodies, and exert higher cytotoxicity effects[39]. The Zn-induced Aβ oligomers can inhibit hippocampal LTP and activate microglia in wild-type mice[39], supporting their potential role in AD pathogenesis. Our NMR data confirm rapid conversion of Aβ monomers to NMR-invisible oligomers upon stoichiometric addition of Zn (the effective Zn concentration could be lower due to the presence of 10 mM phosphate as buffer). Interestingly, this conversion could be partially reverted by the addition of EDTA. The ^{19}F DEST data collected after Zn addition allowed accessing a sub-population of Zn-induced Aβ oligomers, which undergo rapid exchange with Aβ monomers on the millisecond timescale. The exchanging Aβ oligomers are estimated to have an average molecular mass between ~20 and 60 kDa (~5–14 mer), with a relatively rigid N-terminal part due to Zn binding. Unlike larger Zn-induced Aβ aggregates, which are formed irreversibly, these small Aβ oligomers could diffuse relatively rapidly in the human brain and act as zinc ionophores. Accordingly, we speculate that such Zn-induced Aβ oligomers could influence Zn distribution in human brains and thereby contribute to AD pathogenesis by, e.g., reducing Zn ion concentration in glutamatergic synaptic clefts, particularly in the hippocampus and entorhinal cortex, and affecting processes such as synaptic plasticity in those regions[12]. Further studies are required to investigate this hypothesis and explore its potential therapeutic implications, although specific targeting of soluble Zn–Aβ oligomers seems to be extremely challenging due to the current lack of high-resolution structural knowledge on them. Preparation of soluble Zn-stabilized Aβ oligomers, as achieved in a recent report[41], facilitates further structural characterizations. It should be noted that the Zn-bound Aβ oligomeric species undergoing exchange with free Aβ monomers may constitute only a fraction of such Aβ preparations. Considering the peptide and ion concentration dependence of Zn-induced Aβ oligomerization, this process may occur only at specific compartments of the brain (e.g., near synaptic clefts) and for brief periods (e.g., during synaptic firing), where the local Aβ and Zn concentrations can reach high levels.

At sub-stoichiometric concentrations, Zn ions perturb the morphology of Aβ fibrils, potentially through rapid exchange between Aβ molecules and/or formation of structurally distinct aggregation-competent seeds[42]. This is in line with the millisecond lifetime of Zn–Aβ complex obtained through ^{19}F DEST analysis here. At stoichiometric concentrations, Zn ions promote amorphous, rather than fibrillar, aggregation. Despite the structural heterogeneity of Zn-induced Aβ aggregates proposed by solid-state NMR studies[39,43,44], the cross-β hairpin structure in the middle and C-terminal regions of Aβ seems to be largely preserved. Less is known about the structure of the N-terminal region of Aβ within Zn-induced aggregates. Interrogating fluorine NMR and EPR probes at the N-terminal region of Aβ, our results demonstrate that the inter-molecular distance between the N-terminal residue (here, MTSSL-labeled Cys0) and fluorine-labeled aromatic residues (Phe4, Tyr10, Phe19, and Phe20) is greater than ~1.5 nm. Considering the less ordered structure of Zn-induced Aβ aggregates esp. in the N-terminal region, this lower bound for intermolecular distances seems to be compatible with the head-to-head, head-to-tail, and mixed arrangement of Aβ40 molecules within these aggregates (Fig. 8). On the other hand, the bridging model in which Zn is simultaneously coordinated with two Aβ molecules, as suggested in refs. 45,46, is least consistent with our data, because in that scenario the distance between the N-terminal residue and N-terminal fluorinated residues (Tyr10 and esp. Phe4) is expected to be less than 1.5 nm. Recently, a statistical analysis of Zn-binding proteins with binuclear sites revealed Zn–Zn distances range of 0.34–0.39 nm[47]. However,

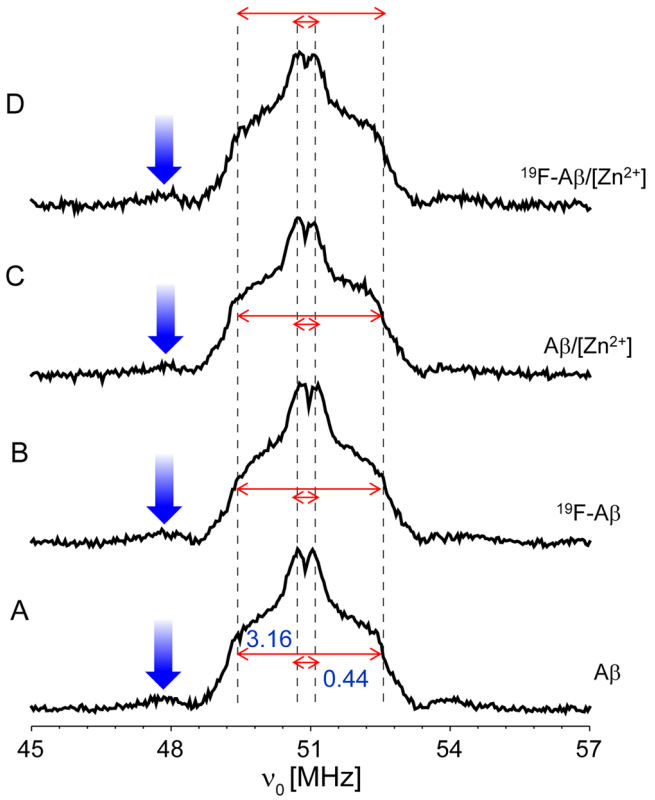

Fig. 6 | Effect of zinc ion on the Mims-ENDOR spectra of Aβ40. The spectra were recorded at 50 K for **A** Aβ40, **B** ^{19}F-Aβ40, **C** Aβ40/[Zn] (1:1), and **D** ^{19}F-Aβ40/[Zn] (1:1). Each Aβ sample contains a 1:1 mixture of MTSSL-labeled Cys-Aβ40 and non-fluorinated (**A**, **C**) or fluorinated (**B**, **D**) Aβ40. Well resolved hyperfine splitting arising from the maxima of Pake patterns is shown, with two coupling values (^{1}H/NO•) of 0.44 and 3.16 MHz. The blue arrows aim to highlight the unmodified spectral region for the entire set of four samples, both with the fluorinated Aβ and the addition of Zn.

in a large number of Zn-binding proteins, mainly dimeric or multi-domain proteins, the inter-ion distances were considerably larger than this range. As examples, in the isonicotinimidylated liver alcohol dehydrogenase (PDB CODE: 7ADH) and the zinc finger antiviral protein in complex with RNA (PDB CODE: 6UEI), the Zn–Zn distances are ~1.9 nm and 1.6–2.9 nm, respectively[48,49]. The Zn–Zn distances in soluble Zn–Aβ oligomers seem to be comparable with these relatively large distances.

Fluorine NMR offers several experimental advantages in terms of signal-to-noise ratio and resolution, as well as sensitivity to detect small conformational/chemical alterations[24,25]. The van der Waals radii of fluorine (1.47 Å) and hydrogen (1.2 Å) atoms are very close; therefore, fluorine atoms are widely regarded as a sterically conservative replacement for hydrogen atoms. However, fluorine atoms have quite distinct electronic properties; consequently, peptide fluorination could potentially alter their structural dynamics and influence their solubility and other properties, including their aggregation. In this study, we prepared recombinant fluorine-labeled Aβ40 and assigned its four ^{19}F NMR signals through chemical synthesis of site-specifically labeled Aβ40. The ^{1}H NMR chemical shift and diffusion data confirmed that the backbone conformation and overall size/shape of Aβ40 were not altered by fluorine labeling. In addition, the EM and ThT fluorescence data confirmed that Aβ40 fluorination did not interfere with its fibrillar aggregation (Fig. S8), and the SEC data demonstrated that the Zn-induced Aβ40 aggregation was similar between the non-fluorinated and fluorinated Aβ40 (Fig. S19). Furthermore, the ^{19}F relaxation data provided dynamical information on the rotational motion of Phe and Tyr rings with τ_c of ~ 1 ns. The combined use of ^{1}H and ^{19}F NMR allowed monitoring Zn binding to Aβ40 and the consequent conversion of Aβ40 monomers to NMR-invisible aggregates. In particular, the ^{19}F DEST method enabled accessing the otherwise NMR-invisible Zn-induced Aβ oligomers undergoing exchange with the NMR-visible Aβ monomers. In addition to the technical advantages, including the easy implementation of 1D ^{19}F DEST methods, the use of ^{19}F probes provided two specific advantages over conventional ^{15}N and ^{13}C probes: first, the higher sensitivity of ^{19}F CSA to conformational/chemical alterations increases the relaxation rate difference between different states, hence facilitates accessing the exchange processes occurring between them at faster timescales[29]; second, the larger dynamics of ^{19}F-labeled side-chains (compared with the ^{15}N- and ^{13}C-labeled peptide backbone) enables capturing larger Aβ species within the pool of NMR-invisible Aβ aggregates. As a complementary technique, the EPR method provided structural information about Aβ aggregates, which remained inaccessible through the use of ^{1}H and ^{19}F NMR methods. A potential limitation of our quantitative results is the use of phosphate buffer, which, as stated above, was chosen due to practical considerations of our solution NMR measurements. Phosphate can act as a strong ligand for Zn and reduce the effective free Zn concentration[19], hence our data should be used with caution under different buffer conditions, or when parameters such as dissociation constant (K_d) or association rate constant (k_{on}) are to be estimated. Future experiments using other buffers such as Tris-HCl and HEPES will allow circumventing the shortcomings of each specific buffer and investigating, at the molecular level, how the choice of buffer could affect the balance between thermodynamic stability and kinetic pathway and alter the structure of Zn-induced Aβ oligomers.

To sum up, we produce recombinant fluorinated Aβ40 and characterize it in the free and Zn-bound states using ^{1}H and especially ^{19}F NMR methods, complemented with the CW EPR and ENDOR methods. Our results support the role of the N-terminal region of Aβ40 as the primary binding site with Zn and the rapid Zn-induced conversion of Aβ monomers to aggregates, which is partially reversible upon Zn chelation. In particular, using the advantages of ^{19}F NMR methods, we provide information about the small soluble Zn-induced Aβ oligomers exchanging with Aβ40 monomers. Due to their potential contribution to AD pathogenesis, these small soluble Zn-induced Aβ oligomers may be considered as druggable target candidates in AD and other neurodegenerative diseases and therefore deserve further structural characterization in future studies.

Methods

Materials

^{19}F-labeled amino acids (4-fluoro-phenylalanine and 3-fluoro-tyrosine) with or without Fmoc groups were purchased from AnaSpec (California, US) and abcr, respectively. Aβ(1–40) and Cys0-Aβ(1–40) were purchased from Bachem ((#4014442, #4034867). The nitroxide spin label (1-Oxyl-2,2,5,5-tetramethyl-3-pyrroline-3-methyl)methanethiosulfonate (MTSSL) was from Toronto Research Chemicals (#O875000).

Recombinant production of fluorinated Aβ

Fluorinated Aβ(1–40) was obtained by recombinant production in defined medium based on the protocol of Gee et al. [26] using *E. coli* DL39(DE3) cells [phenylalanine and tyrosine auxotrophic] transformed with the [NANP]$_{19}$ fusion construct described by Finder and Glockshuber[50] (Fig. S1A). The medium was supplemented with 4-fluoro-phenylalanine and 3-fluoro-tyrosine. The supernatant after sonication and the pellet solubilized in buffer with 8 M guanidinium were both purified by IMAC in the presence of 6 M guanidinium. The flow through was rerun, and the elution peaks from both IMACs were further purified by preparative RP-HPLC, removing the guanidinium. After lyophilization and resolubilisation, the fusion protein was cleaved by adding recombinantly expressed TEV–protease (hexahistidine-tagged). The cleavage products were then again purified by RP-HPLC. The four main peaks were identified by HPLC references, SDS-PAGE, and Western Blot as cleaved NANP19-Linker (1), uncleaved rests of fusion protein (2), F-Phe,F-Tyr-Amyloid beta (1–40) (3), and TEV protease (4) (Fig. S1B–E). Both HPLC purification steps were performed on an Agilent Infinity 1260 system using a ZORBAX SB300-C8 column (Agilent

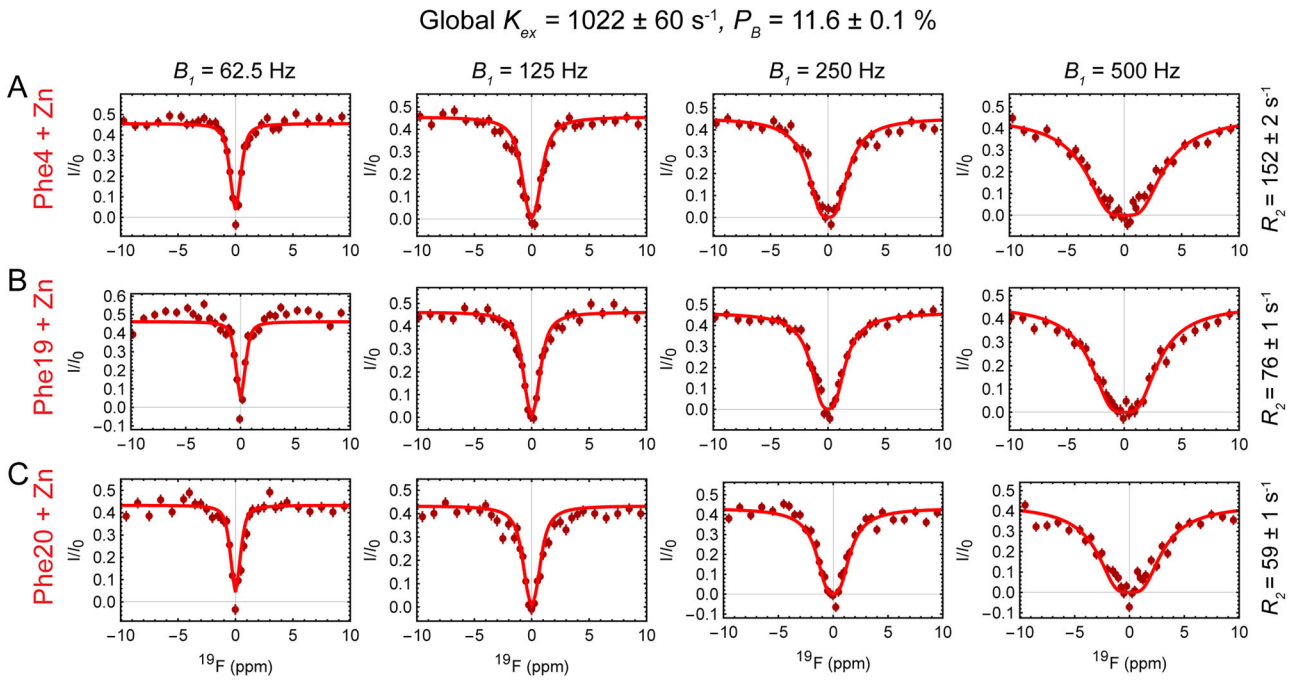

Fig. 7 | ^{19}F DEST profiles of fluorinated Aβ40 in the presence of zinc ion. The profiles were obtained through ^{19}F DEST experiments at four ^{19}F B_1 fields of 62.5, 125, 250, and 500 Hz, for residues Phe4 (**A**), Phe19 (**B**), and Phe20 (**C**). The DEST profiles were acquired for Aβ40 in the presence of equimolar zinc ion, and analyzed assuming a "two-site exchange" model. The experiment was set up to monitor the exchange between monomeric Aβ with a small R_2 ($R_{2,A}$) and an NMR-invisible Zn-induced Aβ oligomeric state with a large R_2 ($R_{2,B}$). The fluorine atoms are substituted at position 4 (para) of Phe. The global k_{ex} and P_B were determined from a two-dimensional grid search, with n = 100 Monte Carlo fittings of stochastic noise added to experimental datasets (details in "Methods"). The $R_{2,B}$ values for the residues are shown on the right. The mean of the 100 MC runs is reported as parameter values, and the standard deviation is reported as uncertainties. The $R_{2,B}$ values for the residues are shown on the right, with standard errors of fit shown as uncertainties. The uncertainties in the data points are the standard deviation from independent experimental measurements (n = 10) as described in Fig. 3.

#880995-206) with an aqueous acetonitrile gradient in the constant presence of 0.1% trifluoroacetic acid (TFA). The Aβ was lyophilized, aliquoted in hexafluoroisopropanol (HFIP), lyophilized again, and stored at −80 °C. The yield was measured by analytical HPLC comparing the absorption at 215 nm to an Aβ(1–40) reference (Fig. S1F). The sequence identity was also confirmed through UHPLC-coupled ESI tandem mass spectrometry (performed at the Molecular Proteomics Laboratory, Medical Faculty and University Hospital Duesseldorf, Heinrich Heine University Duesseldorf), with the most abundantly detected species being the desired full-length Aβ40, fluorinated at all four aromatic amino acid residues (Fig. S1G). The final yield was approximately 1.85 mg from 400 mL defined medium.

Chemical synthesis of fluorinated Aβ

Fluorinated Aβ(1–40) was synthesized in-house on the basis of the Fmoc strategy on a H-Val-HMPB-Chem-Matrix-resin (Sigma Aldrich), using an automated microwave synthesizer (Liberty 1, CEM). Before the chemical synthesis, the reactive side-chain hydroxyl group of Fmoc-3-fluoro-tyrosine was protected as *tert*-butyl ether by treatment with isobutylene and H_2SO_4. Aβ(1–40) peptides with fluorine labels at four (Phe4, Phe19, Phe20, and Tyr10) or one (Phe4, Phe19, or Phe20) positions were synthesized and used for ^{19}F NMR resonance assignment. The HPLC chromatograms and mass spectrometry analyses of the synthesized peptides are shown as Supplementary Figs. S2–S5.

Preparation of MTSSL-labeled Aβ

For preparation of MTSSL-labeled Aβ, 1 mg of Cys0-Aβ(1–40) was dissolved in HFIP and lyophilized again. Then 1 mL of 70% 200 mM HEPES pH = 7.6 and 30% 2 μg/μL MTSSL (freshly dissolved in dimethylformamide) was added, and the sample was incubated for at least 1 h on ice in the dark. The reaction product was purified by RP-HPLC using a ZORBAX SB300-C8 column (Agilent #880995-206) with a 15 min elution gradient from 10% to 36% acetonitrile in the constant presence of 0.1% trifluoroacetic acid (TFA). The labeled peptide was then aliquoted, lyophilized, and stored at −80 °C.

NMR experiments

^{19}F NMR experiments were performed at a 600 MHz Bruker spectrometer (corresponding to ^{19}F Larmor frequency of around 565 MHz) equipped with a cryogenic fluorine-enabled QCI probe. The temperature was set at 278 K. The NMR sample typically contained ~0.2 or 0.5 mg/mL (corresponding to ~46 or 115 μM) Aβ40 (recombinantly produced, unless specified otherwise) and 10 mM sodium phosphate (pH 7.4), to which 0.5 mM DSS was added for proton chemical shift referencing (0.000 ppm). An internal standard (TFA) was used for ^{19}F chemical shift referencing (−76.55 ppm)[51,52]. A more recent reference proposes a value of −75.25 ppm for a TFA-based ^{19}F chemical shift referencing in H_2O/D_2O solvents, but was not used here[53].

2D ^{1}H,^{1}H TOCSY and NOESY spectra were carried out using a 900 MHz Bruker spectrometer with 600 × 16384 complex points in t_1 and t_2 dimensions, with spectral widths of 9090.909 Hz in t_1 and 10869.565 Hz in t_2 dimensions and 16 or 32 scans per t_1 increment for TOCSY and NOESY, respectively. The mixing times were 45, 60, and 75 ms for the TOCSY and 200 and 300 ms for the NOESY experiments.

Diffusion coefficients of fluorinated Aβ40 in the free state and non-fluorinated Aβ40 in the free and Zn-bound states were measured through ^{1}H-based pulse-field-gradient (PFG)-NMR experiments at a 600 MHz Bruker spectrometer. The big and little diffusion delays were set at 200 and 1.4 ms, respectively. Gradients were calibrated using the known diffusion coefficient of the residual HDO in 99.8% D_2O at 25 °C (1.900×10^{-9} m^2 s^{-1}). Intensity attenuation data induced by the magnetic field z-gradients were fitted using the Stejskal–Tanner (ST) equation[54]. The diffusion coefficient of DSS was measured using a big and a little diffusion delay of 100 and 2 ms,

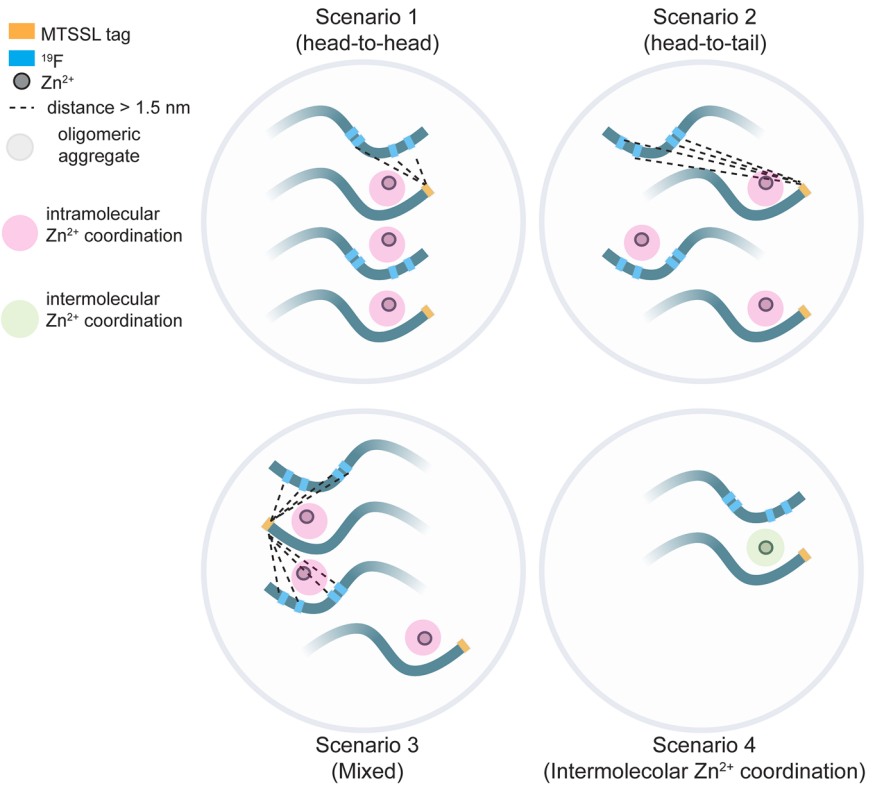

Fig. 8 | Schematic representation of Zn-induced Aβ40 aggregates, as suggested by our data. The "intermolecular" distances of greater than 1.5 nm between the nitroxide spin label (MTSSL) attached to Cys0 at the N-terminus and the fluorine atoms attached at Phe4, Tyr10, Phe19, and Phe20 side-chains seem to be compatible with three possible scenarios of head-to-head (1), head-to-tail (2), and mixed (3) arrangements of Aβ40 molecules within aggregates. The bridging model, scenario (4), in which the Zn^{2+} ion is simultaneously coordinated with two Aβ molecules, is least consistent with our data. It should be noted that in the condition used in our study (100 μM $ZnCl_2$, 10 mM phosphate buffer, pH 7.4, 278 K), free Zn^{2+} ions coexist with other Zn species, which can affect some aspects of Zn-induced Aβ aggregation.

and used as an internal reference for the calculation of Aβ40's hydrodynamic radius.

2D ^{1}H,^{19}F heteronuclear Overhauser effect spectroscopy (HOESY) experiments were acquired with 160 × 32768 complex points in t_1 (^{1}H) and t_2 (^{19}F) dimensions and 696 scans per t_1 increment, with spectral widths of 7804.327 Hz in ^{1}H and 45454.547 in ^{19}F dimensions. A mixing time of 0.5 s was used, and the total relaxation delay (d_1 + AQ, acquisition time) was 1.66 s. The ^{19}F longitudinal relaxation rates were measured through standard inversion–recovery (IR) experiments, using 10 relaxation delays of 0.01, 0.02, 0.04, 0.08, 0.16, 0.32, 0.64, 1.28, 2.56, and 5.12 s. A total relaxation delay of ~4 s was used for the IR experiments. The ^{19}F dark-state exchange saturation transfer (DEST) experiments were performed through a simple pulse-acquire experiment using a DEST block of 0.5 s before the 90° pulse, during which continuous-wave (CW) ^{19}F irradiation at B_1 fields of 62.5, 125, 250, and 500 Hz was applied. The DEST profiles are reported as normalized ^{19}F signal intensities versus chemical shift offset from the interesting signal. The normalization was done using the measured ^{19}F R_1 rates for each signal and the DEST duration of 0.5 s. The rotational correlation time (τ_c) and reduced anisotropy (δ_σ) of fluorine-labeled rings were estimated from ^{19}F relaxation rates using standard equations[55] and n = 100 Monte Carlo runs of grid searches.

DEST analysis

The Bloch–McConnell matrix formalism[56,57] was used to fit the experimental residue-wise fluorine data points (I/I_0) at different B_1 irradiation fields along the ^{19}F ppm axis. The four ^{19}F B_1 fields of 62.5 Hz, 125 Hz, 250 Hz, and 500 Hz were fitted simultaneously. In the case of the Aβ peptide without Zn, the DEST data of each residue were analyzed individually, assuming a "no-exchange" model with parameters R_1 and R_2 for that residue. In the presence of Zn, which drives Aβ oligomer formation, the DEST profiles were analyzed according to a "two-site exchange" model between the free monomeric and Zn-bound oligomeric Aβ. This model contained additional parameters R_{1B} and R_{2B} (relaxation rates of the Zn-bound Aβ), k_{ex} (exchange rate between the free and Zn-bound Aβ), and P_B (population of the Zn-bound form). For fitting the DEST data in the presence of Zn, the R_1 and R_2 values of each residue in the free monomeric Aβ were kept constant and taken from the above analysis, a global exchanging event was assumed (global k_{ex} and P_B), and $\Delta\omega$ (chemical shift difference between the two states) was fixed to 0. The data was fitted using NonlinearModelFit in Mathematica (Version 14.3) (Wolfram 2025) and in-house scripts. The constrained global optimization was performed using the Nelder–Mead method. The uncertainties of the fit parameters for the free Aβ represent the Standard Error of Fit as reported by NonlinearModelFit. Initially, the DEST data were fitted individually for each residue. Next, we constructed a grid of the global parameters k_{ex} (100–5000 s^{-1}) and P_B (2.5–12.5%) that covers all the individual fit results. We used global fitting for the residues in n = 100 independent Monte Carlo runs with initial estimates of k_{ex} and P_B drawn randomly from the above-mentioned grid. For the Monte Carlo runs, we have added stochastic noise sampled from a normal distribution, using a sigma value defined by the experimental uncertainties. The reported parameter values and uncertainties represent the mean and standard deviation of n = 100 Monte Carlo fit results. The parallel implementation of NonlinearModelFit with n = 100 MC runs required about 4 h of computation time on the AMD Ryzen 9 7900 12-Core Processor (3.70 GHz) computer with 32 GB RAM.

EPR experiments

Samples containing solutions of Aβ40 and the mixtures Aβ40/Zn were filled into 1.8 mm (outer diameter) quartz tubes and shock frozen in liquid nitrogen for EPR measurements for the Mims-ENDOR experiments. The same tubes had been used for CW EPR experiments before freezing. Continuous wave (CW) EPR spectra were recorded at X-band (ca. 9.5 GHz) on an ElexSys E580 EPR spectrometer (Bruker Biospin, Rheinstetten, Germany) equipped with a rectangular resonator (Bruker SHQ) at room temperature (295 K). Spectra were acquired under non-saturating conditions with a microwave power of 0.2 mW, a B-field modulation amplitude for lock-in detection of 0.05 mT, and a conversion time of 81.92 ms using 1024 points.

Two-pulse (Hahn) echo detected Q-band (34 GHz) EPR spectra were collected with a π/2–τ–π–τ–echo pulse sequence on a Bruker Elexsys-580

using an EN 5107D2 resonator and a HA8019 10 W amplifier. A temperature of 70 K was maintained with an Oxford liquid helium cryostat. The spectra were collected with the following parameters: $\pi = 16$ ns, $\tau = 204$ ns, repetition rate = 2 ms, shots per point = 10, and number of points = 4096; number of scans = 1–10 (Echo-Detected-Field-Swept spectra are reported in Fig. S25).

Mims ENDOR spectra were obtained with the Mims sequence $\pi/2$–τ–$\pi/2$–t_{wait}–T_{RF}–t_{wait}–$\pi/2$–τ–echo at 70 K and the following parameters: $\pi/2 = 16$ ns; $\tau = 200$ ns; $T_{RF} = 25$ ms; $t_{wait} = 2$ ms; repetition time = 2 ms; shots per point = 1; number of points = 1024; number of scans = ~25,000 (depending on sample). The RF pulse frequency (600 W Vectawave RF amplifier) was randomly hopped without phase cycling.

Data availability

All data needed to evaluate the conclusions are present in the paper or in the Supplementary Information or available upon request from the corresponding author. The source data for Figs. 1G, 2, 3, and 7 are provided as Supplementary Data 1. All DEST data and corresponding Mathematica notebooks are included as a zipped Supplementary Data 2.

Received: 2 November 2025; Accepted: 29 June 2026;
Published online: 13 July 2026

References

1. Barnham, K. J. & Bush, A. I. Metals in Alzheimer's and Parkinson's diseases. *Curr. Opin. Chem. Biol.* **12**, 222–228 (2008).
2. Hopt, A. et al. Methods for studying synaptosomal copper release. *J. Neurosci. Methods* **128**, 159–172 (2003).
3. Faller, P. & Hureau, C. Bioinorganic chemistry of copper and zinc ions coordinated to amyloid-beta peptide. *Dalton Trans*. **38**, 1080–1094 (2009).
4. Tougu, V. & Palumaa, P. Coordination of zinc ions to the key proteins of neurodegenerative diseases: Aβ, APP, α-synuclein and PrP. *Coordin. Chem. Rev.* **256**, 2219–2224 (2012).
5. Atrian-Blasco, E. et al. Cu and Zn coordination to amyloid peptides: from fascinating chemistry to debated pathological relevance. *Coord. Chem. Rev.* **375**, 38–55 (2018).
6. Miller, L. M. et al. Synchrotron-based infrared and X-ray imaging shows focalized accumulation of Cu and Zn co-localized with beta-amyloid deposits in Alzheimer's disease. *J. Struct. Biol.* **155**, 30–37 (2006).
7. Zatta, P., Drago, D., Bolognin, S. & Sensi, S. L. Alzheimer's disease, metal ions and metal homeostatic therapy. *Trends Pharmacol. Sci.* **30**, 346–355 (2009).
8. Lee, J. Y., Cole, T. B., Palmiter, R. D., Suh, S. W. & Koh, J. Y. Contribution by synaptic zinc to the gender-disparate plaque formation in human Swedish mutant APP transgenic mice. *Proc. Natl. Acad. Sci. USA* **99**, 7705–7710 (2002).
9. Okafor, M., Faller, P. & Vitale, N. Cell-specific copper dyshomeostasis mechanism in Alzheimer's disease. *Transl. Neurodegener.* **14**, 42 (2025).
10. Bush, A. I. & Tanzi, R. E. Therapeutics for Alzheimer's disease based on the metal hypothesis. *Neurotherapeutics* **5**, 421–432 (2008).
11. Shippy, D. C., Oliai, S. F. & Ulland, T. K. Zinc utilization by microglia in Alzheimer's disease. *J. Biol. Chem.* **300**, 107306 (2024).
12. Lee, K., Mills, Z., Cheung, P., Cheyne, J. E. & Montgomery, J. M. The role of zinc and NMDA receptors in autism spectrum disorders. *Pharmaceuticals (Basel)* **16**, 1 (2022).
13. Atrian-Blasco, E., Conte-Daban, A. & Hureau, C. Mutual interference of Cu and Zn ions in Alzheimer's disease: perspectives at the molecular level. *Dalton Trans.* **46**, 12750–12759 (2017).
14. Alies, B. et al. Zinc(II) binding site to the amyloid-β peptide: insights from SPectroscopic Studies with A Wide Series of Modified Peptides. *Inorg. Chem.* **55**, 10499–10509 (2016).
15. Alies, B. et al. Mutations of histidine 13 to arginine and arginine 5 to glycine are responsible for different coordination sites of zinc(II) to human and murine peptides. *Chemistry* **24**, 14233–14241 (2018).
16. Radko, S. P. et al. The English (H6R) mutation of the Alzheimer's disease amyloid-beta peptide modulates its zinc-induced aggregation. *Biomolecules* **10**, 961 (2020).
17. Yao, S., Flight, R. M., Rouchka, E. C. & Moseley, H. N. A less-biased analysis of metalloproteins reveals novel zinc coordination geometries. *Proteins* **83**, 1470–1487 (2015).
18. Bazayeva, M., Andreini, C. & Rosato, A. A database overview of metal-coordination distances in metalloproteins. *Acta Crystallogr. D Struct. Biol.* **80**, 362–376 (2024).
19. Krężel, A. & Maret, W. The biological inorganic chemistry of zinc ions. *Arch. Biochem. Biophys.* **611**, 3–19 (2016).
20. Danielsson, J., Pierattelli, R., Banci, L. & Graslund, A. High-resolution NMR studies of the zinc-binding site of the Alzheimer's amyloid beta-peptide. *FEBS J.* **274**, 46–59 (2007).
21. Rezaei-Ghaleh, N., Giller, K., Becker, S. & Zweckstetter, M. Effect of zinc binding on beta-amyloid structure and dynamics: implications for Abeta aggregation. *Biophys. J.* **101**, 1202–1211 (2011).
22. Kozin, S. A. et al. The English (H6R) familial Alzheimer's disease mutation facilitates zinc-induced dimerization of the amyloid-beta metal-binding domain. *Metallomics* **7**, 422–425 (2015).
23. Vemulapalli, S. P. B., Becker, S., Griesinger, C. & Rezaei-Ghaleh, N. Combined high-pressure and multiquantum NMR and molecular simulation propose a role for N-terminal salt bridges in amyloid-beta. *J. Phys. Chem. Lett.* **12**, 9933–9939 (2021).
24. Gronenborn, A. M. Small, but powerful and attractive: F in biomolecular NMR. *Structure* **30**, 6–14 (2022).
25. Kitevski-LeBlanc, J. L. & Prosser, R. S. Current applications of F NMR to studies of protein structure and dynamics. *Prog. Nucl. Magn. Reson. Spectrosc.* **62**, 1–33 (2012).
26. Gee, C. T. et al. Protein-observed (19)F-NMR for fragment screening, affinity quantification and druggability assessment. *Nat. Protoc.* **11**, 1414–1427 (2016).
27. Russo, L. et al. Direct detection of an NH-π hydrogen bond in an intrinsically disordered peptide. *Nat. Commun.* **16**, 10231 (2025).
28. Beyer, I. et al. Solid-phase synthesis and characterization of N-terminally elongated abeta-3-x -peptides. *Chemistry* **22**, 8685–8693 (2016).
29. Tugarinov, V., Ceccon, A. & Clore, G. M. NMR methods for exploring 'dark' states in ligand binding and protein-protein interactions. *Prog. Nucl. Magn. Reson. Spectrosc.* **128**, 1–24 (2022).
30. Rezaei-Ghaleh, N., Parigi, G. & Zweckstetter, M. Reorientational dynamics of amyloid-beta from NMR spin relaxation and molecular simulation. *J. Phys. Chem. Lett.* **10**, 3369–3375 (2019).
31. Durr, U. H., Grage, S. L., Witter, R. & Ulrich, A. S. Solid state 19F NMR parameters of fluorine-labeled amino acids. Part I: aromatic substituents. *J. Magn. Reson.* **191**, 7–15 (2008).
32. Hull, W. E. & Sykes, B. D. Fluorotyrosine alkaline phosphatase: internal mobility of individual tyrosines and the role of chemical shift anisotropy as a 19F nuclear spin relaxation mechanism in proteins. *J. Mol. Biol.* **98**, 121–153 (1975).
33. Meyer, A., Dechert, S., Dey, S., Hobartner, C. & Bennati, M. Measurement of angstrom to nanometer molecular distances with (19) F nuclear spins by EPR/ENDOR spectroscopy. *Angew. Chem. Int. Ed. Engl.* **59**, 373–379 (2020).
34. Matei, E. & Gronenborn, A. M. 19)F Paramagnetic Relaxation Enhancement: A Valuable Tool for Distance Measurements in Proteins. *Angew. Chem. Int. Ed. Engl.* **55**, 150–154 (2016).
35. Branch, T., Barahona, M., Dodson, C. A. & Ying, L. Kinetic Analysis Reveals the Identity of Abeta-Metal Complex Responsible for the Initial Aggregation of Abeta in the Synapse. *ACS Chem. Neurosci.* **8**, 1970–1979 (2017).

36. Kayed, R. et al. Common structure of soluble amyloid oligomers implies common mechanism of pathogenesis. *Science* **300**, 486–489 (2003).
37. Brettschneider, J., Del Tredici, K., Lee, V. M. & Trojanowski, J. Q. Spreading of pathology in neurodegenerative diseases: a focus on human studies. *Nat. Rev. Neurosci.* **16**, 109–120 (2015).
38. Langer, F. et al. Soluble Abeta seeds are potent inducers of cerebral beta-amyloid deposition. *J. Neurosci.* **31**, 14488–14495 (2011).
39. Lee, M. C. et al. Zinc ion rapidly induces toxic, off-pathway amyloid-beta oligomers distinct from amyloid-beta derived diffusible ligands in Alzheimer's disease. *Sci. Rep.* **8**, 4772 (2018).
40. Dahlgren, K. N. et al. Oligomeric and fibrillar species of amyloid-beta peptides differentially affect neuronal viability. *J. Biol. Chem.* **277**, 32046–32053 (2002).
41. Gonzalez Diaz, A., Cataldi, R., Mannini, B. & Vendruscolo, M. Preparation and characterization of Zn(II)-stabilized abeta(42) oligomers. *ACS Chem. Neurosci.* **15**, 2586–2599 (2024).
42. Matheou, C. J., Younan, N. D. & Viles, J. H. The rapid exchange of Zinc(2+) enables trace levels to profoundly influence amyloid-beta misfolding and dominates assembly outcomes in Cu(2+)/Zn(2+) mixtures. *J. Mol. Biol.* **428**, 2832–2846 (2016).
43. Mithu, V. S. et al. Zn(++) binding disrupts the Asp(23)-Lys(28) salt bridge without altering the hairpin-shaped cross-beta Structure of Abeta(42) amyloid aggregates. *Biophys. J.* **101**, 2825–2832 (2011).
44. Chandra, B. et al. Curcumin dictates divergent fates for the central salt bridges in amyloid-beta(40) and amyloid-beta(42). *Biophys. J.* **112**, 1597–1608 (2017).
45. Kozin, S. A. et al. Zinc-induced dimerization of the amyloid-β metal-binding domain 1-16 is mediated by residues 11-14. *Mol. Biosyst.* **7**, 1053–1055 (2011).
46. Miller, Y., Ma, B. & Nussinov, R. Zinc ions promote Alzheimer Abeta aggregation via population shift of polymorphic states. *Proc. Natl. Acad. Sci. USA* **107**, 9490–9495 (2010).
47. Mechtinger, G., Axel, G., Kolodny, R. & Ben-Tal, N. Interpretable prediction of zinc ion location in proteins with ZincSight. *Protein Sci.* **34**, e70350 (2025).
48. Plapp, B. V., Eklund, H., Jones, T. A. & Branden, C. I. Three-dimensional structure of isonicotinimidylated liver alcohol dehydrogenase. *J. Biol. Chem.* **258**, 5537–5547 (1983).
49. Meagher, J. L. et al. Structure of the zinc-finger antiviral protein in complex with RNA reveals a mechanism for selective targeting of CG-rich viral sequences. *Proc. Natl. Acad. Sci. USA* **116**, 24303–24309 (2019).
50. Finder, V. H., Vodopivec, I., Nitsch, R. M. & Glockshuber, R. The recombinant amyloid-beta peptide Abeta1-42 aggregates faster and is more neurotoxic than synthetic Abeta1-42. *J. Mol. Biol.* **396**, 9–18 (2010).
51. Jiang, Z. X., Feng, Y. & Yu, Y. B. Fluorinated paramagnetic chelates as potential multi-chromic 19F tracer agents. *Chem. Commun. (Camb.)* **47**, 7233–7235 (2011).
52. Yu, J. X., Hallac, R. R., Chiguru, S. & Mason, R. P. New frontiers and developing applications in 19F NMR. *Prog. Nucl. Magn. Reson. Spectrosc.* **70**, 25–49 (2013).
53. Rosenau, C. P., Jelier, B. J., Gossert, A. D. & Togni, A. Exposing the origins of irreproducibility in fluorine NMR Spectroscopy. *Angew. Chem. Int. Ed. Engl.* **57**, 9528–9533 (2018).
54. Hrabe, J., Kaur, G. & Guilfoyle, D. N. Principles and limitations of NMR diffusion measurements. *J. Med. Phys.* **32**, 34–42 (2007).
55. Kitevski-LeBlanc, J. L. & Prosser, R. S. Current applications of 19F NMR to studies of protein structure and dynamics. *Prog. Nucl. Magn. Reson. Spectrosc.* **62**, 1–33 (2012).
56. Abergel, D. & Palmer, A. G. Approximate solutions of the Bloch-McConnell equations for two-site chemical exchange. *Chemphyschem* **5**, 787–793 (2004).
57. Eykyn, T. R., Elliott, S. J. & Kuchel, P. W. Extended Bloch-McConnell equations for mechanistic analysis of hyperpolarized (13)C magnetic resonance experiments on enzyme systems. *Magn. Reson. (Gott)* **2**, 421–446 (2021).

Acknowledgements

N.R.-G. acknowledges the Department of Molecular Medicine, University of Pavia, for a starting grant (as part of the "Progetto di eccellenza 2023/2027"). N.R.-G. acknowledges the Deutsche Forschungsgemeinschaft (German Research Foundation, DFG) for the research grant RE 3655/2-3. D.W. and N.R.-G. acknowledge the DFG for a grant under the project number 497967936. G.S. and S.G. acknowledge IR INFRANALYTICS FR2054 for financial support. K.S.C. thanks the Krea Research Fellowship 23–24 and Krea University for the computational facility. We thank Dr. Lothar Gremer for technical suggestions in recombinant preparation of fluorinated Aβ peptide, Dr. Anja Stefanski from Molecular Proteomics Laboratory, Medical Faculty and University Hospital Duesseldorf, Heinrich Heine University Duesseldorf, for mass spectrometry experiments and analyses, and Dr. Dietmar Riedel and the Synthetic Chemistry facility of the Max Planck Institute for Multidisciplinary Sciences, Goettingen, respectively, for the EM examination of Aβ samples and for the synthesis of protected Fmoc-fluoro-Tyr used for chemical synthesis of fluorinated Aβ.

Author contributions

Conceptualization, Funding acquisition, Supervision, Writing—original draft: N.R.-G. Resources: N.R.-G., R.B., K.O., G.S., K.C., and D.W. Investigation: N.R.-G., L.R., R.B., S.G., and G.S. Formal analysis: N.R.-G., L.R., K.C., and G.S. Visualization: N.R.-G., L.R., K.C., R.B., K.O., and G.S. Writing—review and editing: all the authors.

Competing interests

The authors declare no competing interests.

Additional information

Supplementary information The online version contains supplementary material available at https://doi.org/10.1038/s42004-026-02121-4.

Correspondence and requests for materials should be addressed to Nasrollah Rezaei-Ghaleh.

Peer review information *Communications Chemistry* thanks the anonymous reviewers for their contribution to the peer review of this work. A peer review file is available.

Reprints and permissions information is available at http://www.nature.com/reprints

Publisher's note Springer Nature remains neutral with regard to jurisdictional claims in published maps and institutional affiliations.

Open Access This article is licensed under a Creative Commons Attribution-NonCommercial-NoDerivatives 4.0 International License, which permits any non-commercial use, sharing, distribution and reproduction in any medium or format, as long as you give appropriate credit to the original author(s) and the source, provide a link to the Creative Commons licence, and indicate if you modified the licensed material. You do not have permission under this licence to share adapted material derived from this article or parts of it. The images or other third party material in this article are included in the article's Creative Commons licence, unless indicated otherwise in a credit line to the material. If material is not included in the article's Creative Commons licence and your intended use is not permitted by statutory regulation or exceeds the permitted use, you will need to obtain permission directly from the copyright holder. To view a copy of this licence, visit http://creativecommons.org/licenses/by-nc-nd/4.0/.

© The Author(s) 2026